Secondary Organic Aerosols Derived from Intermediate Volatility n-Alkanes Adopt Low Viscous Phase State

Tommaso Galeazzo[1], Bernard Aumont[2], Marie Camredon[2], Richard Valorso[2], Yong B. Lim[3], Paul J. Ziemann[4,5], and Manabu Shiraiwa[1,*]

1. Department of Chemistry, University of California, Irvine, CA92625, USA

2. Univ Paris Est Creteil and Université Paris Cité, CNRS, LISA, F-94010 Créteil, France

3. California Air Resources Board, Riverside, CA92507, USA

4. Department of Chemistry, University of Colorado, Boulder, Colorado, USA

5. Cooperative Institute for Research in Environmental Sciences (CIRES), University of Colorado, Boulder, Colorado, USA

* Correspondence to: m.shiraiwa@uci.edu

Abstract.

Secondary organic aerosol (SOA) derived from n-alkanes, as emitted from vehicles and volatile chemical products, is a major component of anthropogenic particulate matter, yet its chemical composition and phase state are poorly understood and hardly constrained in aerosol models. Here we provide a comprehensive analysis of n-alkane SOA by explicit gas-phase chemistry modeling, machine learning, and laboratory experiments to show that n-alkane SOA adopt low viscous semisolid or liquid states. Our study underlines the complex interplay of molecular composition and SOA viscosity: n-alkane SOA with higher carbon number mostly consists of less functionalized first-generation products with lower viscosity, while the lower carbon number SOA contains more functionalized multigeneration products with higher viscosity. This study opens up a new avenue for analysis of SOA processes and the results indicate little kinetic limitations of mass accommodation in SOA formation, supporting the application of equilibrium partitioning for simulating n-alkane SOA formation in large-scale atmospheric models.

Introduction

Secondary organic aerosols (SOA) are ubiquitous in the atmosphere, affecting climate, air quality and public health (Pöschl and Shiraiwa, 2015; Jimenez et al., 2009). They are generally formed by multigenerational oxidation of volatile organic compounds (VOCs) emitted by both anthropogenic and biogenic sources followed by condensation of semi-volatile oxidation products into the particle phase (Ziemann and Atkinson, 2012; Kroll and Seinfeld, 2008). As an important class of SOA precursors, there is a growing attention to intermediate volatile organic compounds (IVOCs), which can partition to the gas phase upon dilution of primary organic aerosols after fresh emission sources such as vehicle tailpipes, combustion of fossil and fuel oils, and volatile chemical products (Robinson et al., 2007; McDonald et al., 2018). The inclusion of IVOCs in the model simulations helps to reduce the gap between model simulation and field observation of SOA (de Gouw et al., 2011; Li et al., 2022; Zhao et al., 2016).

SOA can adopt different particle phase states (liquid, amorphous semisolid, and glassy solid), depending on their chemical composition, relative humidity and temperature (Virtanen et al., 2010; Petters et al., 2019; Reid et al., 2018; Renbaum-Wolff et al., 2013) and also evolving upon chemical aging and photochemistry (Baboomian et al., 2022). SOA phase state plays an important role in a number of atmospheric multiphase processes (Shiraiwa et al., 2017). The occurrence of glassy SOA in the free troposphere can impact activation pathways of ice crystals and cloud droplets (Knopf and Alpert, 2023). Slow diffusion in viscous particles

51 induces kinetic limitations in heterogeneous and multiphase reactions (Zhang et al., 2018; Zhou

52 et al., 2019; Shiraiwa et al., 2011), affecting long-range transport (Shrivastava et al., 2017; Mu

53 et al., 2018). The timescale of SOA partitioning can be prolonged in viscous particles

54 (Schervish and Shiraiwa, 2023), retarding uptake of semi-volatile compounds and mixing of

55 different particle populations (Ye et al., 2016). Particle phase state also modulates SOA growth

56 to cloud condensation nuclei sizes, affecting cloud life cycle (Zaveri et al., 2022). While the

57 phase states of SOA generated by biogenic VOCs such as terpenes and isoprene have been

58 extensively studied (Virtanen et al., 2010; Petters et al., 2019; Renbaum-Wolff et al., 2013;

59 Baboomian et al., 2022; Zhang et al., 2018), those derived from IVOCs are hardly investigated

60 and remain poorly constrained.

61   Viscosity (η) is a dynamic property that characterizes the particle phase state, which can

62 be derived from the glass transition temperature (T_g) of the constituting species (Koop et al.,

63 2011). Several structure-activity relationships models have been developed to predict the T_g of

64 an organic compound using various molecular properties including molar mass, atomic O:C

65 ratio (Shiraiwa et al., 2017), elemental composition (DeRieux et al., 2018), and volatility (Li et

66 al., 2020; Zhang et al., 2019). A method was developed to predict SOA viscosity from the T_g -

67 scaled Arrhenius plot of fragility by considering Gordon-Taylor mixing rule and hygroscopic

68 growth of SOA particles (DeRieux et al., 2018; Shiraiwa et al., 2017). The T_g compositional

69 parameterizations (CP) and the viscosity prediction method have been applied to high

70 resolution mass spectrometry data of various types of SOA including toluene SOA (DeRieux

71 et al., 2018), SOA generated by diesel fuels (Song et al., 2019), β-caryophyllene SOA (Maclean

72 et al., 2021), and SOA generated by surrogate VOC mixtures by healthy and stressed plants

73 (Smith et al., 2021), agreeing well with viscosity measurements. However, CP substantially

74 overestimated viscosity measurements of indoor surface films which are mostly composed of

75 unsaturated high molar mass compounds such as triglycerides (O'Brien et al., 2021). CP does

76 not consider molecular structure nor functionality explicitly, representing a limitation of this

77 method. Galeazzo and Shiraiwa (2022) overcame this limitation by developing a machine

78 learning-based model, tgBoost, with an application of cheminformatics "molecular

79 embeddings" that retains detailed information on atomic composition, molecular structure and

80 connectivity. The main novel feature introduced by tgBoost is model capability to predict

81 different T_g for structural isomers and high sensitivity of T_g to various functional groups,

82 consistent with viscosity measurements for functionalized compounds (Rothfuss and Petters,

83 2017; Grayson et al., 2017).

84   Long-chain linear alkanes (n-alkanes) are representative IVOCs and account for a

85   substantial fraction of non-methane hydrocarbons in urban air as mainly emitted from

86   anthropogenic activities such as vehicle exhausts and incomplete fuel combustion (Li et al.,

87   2022). Gas-phase oxidation of n-alkanes by OH radicals can trigger the formation of SOA with

88   high yields, as observed in laboratory experiments (Aimanant and Ziemann, 2013a; Lim and

89   Ziemann, 2009b; Srivastava et al., 2022) and field observations (Gentner et al., 2012; Li et al.,

90   2022). Gas-phase oxidation pathways of n-alkanes are relatively well understood and

91   successfully simulated by detailed gas-phase chemistry modeling (Aumont et al., 2012; La et

92   al., 2016), but the chemical composition of n-alkane SOA has only been characterized well for

93   the C_{16} n-alkane (Ranney et al., 2023) and the phase state and viscosity of alkane SOA are

94   unknown. Therefore, the n-alkane SOA system provides an ideal benchmark for the

95   investigation of the interplay of chemical composition, particle phase state and kinetic

96   limitations influencing SOA growth and evolution.

97   In this study, we implemented tgBoost in an explicit gas-phase chemistry model

98   GECKO-A to investigate the complex interplay of chemical composition, kinetic partitioning,

99   and phase state of n-alkane SOA generated under dry and high NOx conditions. The GECKO-

100   A model is one of the most comprehensive generators of gas-phase chemical schemes to date,

101   as it automatically generates detailed gas-phase chemical mechanisms involving thousands to

102   millions of oxidation products from a given VOC precursor based on established reaction

103   pathways and structure–activity relationships (Aumont et al., 2012; La et al., 2016). The

104   simulations were conducted with variable effective mass accommodation coefficient to

105   consider potential kinetic limitations in amorphous semisolid particles (Shiraiwa and Pöschl,

106   2021). The simulated results were compared with chamber experimental data on SOA yields

107   (Lim and Ziemann, 2009b) as well as new measurements on thermal desorption temperatures

108   and functional group distributions.

109

110   **Methods:**

111   **Model simulations.**

112   We applied the Generator for Explicit Chemistry and Kinetics of the Organics in the

113   Atmosphere (GECKO-A) (Aumont et al., 2012; La et al., 2016) to obtain detailed reaction

114   schemes of gas-phase OH oxidation of n-alkanes along with rate constants. The GECKO-A

115   generator used for the oxidation of linear n-alkanes treats chemistry of peroxy (RO_2) and alkoxy

116   (RO) radicals. Under high NOx conditions, RO_2 radicals mainly react with NO and NO_2, to

117   form closed-shell compounds or RO radicals, which undergo reaction with O_2, unimolecular

118   decomposition (i.e. C-C bond breaking) or isomerization, generating stable compounds and/or

119   to new RO_2 radicals. The detailed protocol for such mechanism generation is available in

120   previous studies (Aumont et al., 2013; Aumont et al., 2005; Aumont et al., 2012; La et al.,

121   2016). In this study, the generated chemical schemes include the description of the formation

122   of organic species up to four generations. Species with vapor pressure below 10^{-13} atm are

123   assumed to be of low enough volatility to completely partition to the condensed phase and their

124   gas phase chemistry is then not generated in the mechanism to reduce the mechanism (La et al.,

125   2016). The number of species treated in the model was ~10^4 species for dodecane (C_8H_{18}) that

126   increases to ~10^5 species for heptadecane ($C_{17}H_{36}$).

127   The latest structure-activity relationships are treated for the chemistry of organic

128   compounds with OH radical (Jenkin et al., 2018b, a; Jenkin et al., 2019), the bimolecular

129   reactions of peroxy radicals (Jenkin et al., 2019), as well as alkoxy radical decomposition and

130   H migration reaction rates (Vereecken and Peeters, 2009; La et al., 2016). The vapor pressures

131   of semi-volatile species were estimated by using Nannoolal's group contribution method

132   (Nannoolal et al., 2008) implemented in GECKO-A, as described in detail in Valorso et al.

133   (2011). The model treats unimolecular particle-phase reactions including cyclization of

134   hydroxyketones and dehydration of cyclic hemiacetals to form dihydrofurans (La et al., 2016).

135   The model does not treat autoxidation and dimerization in the gas phase, but these processes

136   should be minor pathways during n-alkane oxidation in the presence of high NOx as the reaction

137   of peroxy radicals with NOx should be dominant (Praske et al., 2018; Pye et al., 2019); thus,

138   their absence from GECKO-A chemical schemes should not have major impacts on the

139   simulated results.

140   These explicit chemical mechanisms were implemented into a box model to simulate

141   the multigenerational oxidation of n-alkanes, partitioning of oxidation products into the particle

142   phase based on their vapor pressures, and vapor wall loss to mimic chamber experiments (La

143   et al., 2016). We replicated the experimental conditions used in Lim and Ziemann (2009b) to

144   generate SOA from OH oxidation of C_8-C_{17} n-alkanes at high NO_x conditions in the presence

145   of non-volatile dioctyl sebacate (DOS) seed particles with particle radius of 150 nm and mass

146   loading of 200 $\mu g\ m^{-3}$. Temperature was held constant at 295.15 K, pressure was set at 1 atm

147   and RH was fixed at 0.5%. Photolysis frequencies were calculated based on the cross sections,

148   quantum yields as described in Aumont et al. (2005) and the photonic flux of blacklight lamps.

149   Each simulation ran for 1 hour and the time evolution of species concentration were computed

150   through a two-step method that solves stiff ordinary differential equations (Verwer, 1994;

151   Verwer et al., 1996). To investigate effects of mass concentrations, we also simulated

experiments of n-alkane photooxidation under high NO_x conditions with low mass loadings by Presto et al. (2010). The number concentration of seed particles with particle diameter of 200 nm was ~5000 cm^{-3}, corresponding to the mass concentration of ~20 µg m^{-3}. Initial mixing ratios of n-alkane and NO_x were in the range of 3 – 99 ppb and 1 – 5 ppm, respectively, as reported in Presto et al. (2010) and these conditions were applied in the model.

The box model accounts for mass transfer kinetics of organic species between gas and particle phases. Partitioning follows Raoult's law at equilibrium and partitioning kinetics is described by the gas-particle mass transfer coefficient with the Fuchs-Sutugin approach (Seinfeld and Pandis, 2016). For the base case scenario, we fixed the mass accommodation coefficient (α) to be 1 based on molecular dynamics simulations (Julin et al., 2014), assuming particles being low viscous liquids without kinetic limitations of bulk diffusion. To account for potential kinetic limitations in viscous particles, we applied an effective mass accommodation coefficient (α_{eff}) that is a function of volatility and bulk diffusivity (Shiraiwa and Pöschl, 2021):

$$\alpha_{eff} = \alpha_s \frac{1}{1+\frac{\alpha_s}{4}\frac{\omega}{D_b}\frac{C^0}{\rho_p}\frac{r_p}{5}\cdot 10^{-12}\frac{g\ cm^{-3}}{\mu g\ m^{-3}}} \tag{1}$$

where α_s is the surface accommodation coefficient assumed to be 1, ω (cm s^{-1}) is the mean thermal velocity of the organic compound in the gas phase, r_P (cm) is the particle radius, ρ_p (g cm^{-3}) is the particle density, and C^0 (µg m^{-3}) is the pure compound saturation mass concentration. D_b (cm^2 s^{-1}) is bulk diffusivity as simulated by conversion of viscosity as detailed below. α_{eff} values are shown as a function of D_b and vapor pressure p^o in Fig A3a. We accounted for a reversible gas-to-chamber wall partitioning of gases and assumed a fixed first-order deposition rate constant of 5×10^{-4} s^{-1} based on experimental observations and previous modeling studies (Krechmer et al., 2016; La et al., 2016; Lim and Ziemann, 2009b). A desorption rate constant from wall to the gas phase was derived by using a parameter of $C_w/M_w\gamma_w$ of 9 µmole m^{-3} for n-alkanes and 120 µmole m^{-3} for oxidation products based on chamber observations (Matsunaga and Ziemann, 2010), as discussed in La et al. (2016). Potential concentration gradients in the particle phase are not resolved explicitly and SOA particles are assumed to be homogeneously well-mixed implicitly.

The glass transition temperatures (T_g) of organic compounds were predicted by the machine learning-based model tgBoost (Galeazzo and Shiraiwa, 2022) and the parameterization based on elemental composition (DeRieux et al., 2018; Li et al., 2020). The implementation of the compositional parametrization into the GECKO-A box model was done in Galeazzo et al. (2021) with a thorough description of all the equations, assumptions and steps

184   adopted for the implementation of this viscosity estimation method. In this study, we

185   implemented tgBoost, a newly developed machine learning model for better predictions of T_g.

186   tgBoost is a powerful model that can discern compositional isomers by functionality and predict

187   the glass transition temperature of an organic compound i ($T_{g,i}$) with an uncertainty of ± 18.3 K

188   using the canonical SMILES notation of a molecule (Galeazzo and Shiraiwa, 2022). We have

189   implemented a pipeline (i.e., gecko2vec) into GECKO-A to predict T_g of compounds from the

190   chemical mechanism in a fast and computationally efficient manner. Gecko2vec executes three

191   main steps: first, it translates the IDs of the compounds of interest of the GECKO-A mechanism

192   into the respective canonical SMILES notations (translation step); second, it transforms the

193   canonical SMILES notations into the respective molecular embeddings (i.e., unique 300-

194   dimensional numerical representations of molecules; embedding step); and finally, the

195   pretrained tgBoost model and its weights are loaded and used to predict T_g of each species

196   (prediction step). Within the box model, the T_g of total SOA particles ($T_{g,org}$) resulting from the

197   combination of its organic component and water mixture is computed using the Gordon–Taylor

198   equation (Dette et al., 2014; Koop et al., 2011; Zobrist et al., 2008). $T_{g,org}$ can be converted to

199   viscosity based on the Vogel-Tammann-Fulcher approach assuming the fragility parameter of

200   10 (DeRieux et al., 2018). Viscosity is further converted into bulk diffusivity using the

201   fractional Stokes-Einstein equation with a fractional parameter of 0.93 and an effective

202   molecular radius of 0.5 nm (Evoy et al., 2019). For both model simulations with CP and

203   tgBoost, the particle number concentration is assumed to remain constant (coagulation is not

204   treated), while the particle radius evolves following the partitioning of organic compounds.

205

206   **Laboratory experiments.**

207   SOA particles were generated from OH oxidation of C_8-C_{17} n-alkanes in a 5.9 m^3 Teflon

208   environmental chamber filled with clean air under high NO_x conditions in the presence of non-

209   volatile dioctyl sebacate (DOS) seed particles, as described in detail elsewhere (Lim and

210   Ziemann, 2009b). Briefly, 1 ppm of n-alkane, 10 ppm of methyl nitrite, and 10 ppm of NO were

211   added to the chamber from a glass bulb, and ~200–400 µg m^{-3} of seed particles were added

212   from an evaporation-condensation apparatus. Relatively high mass concentrations of seed

213   particles were used so that semi-volatile compounds would condense to particles, minimizing

214   vapor deposition to chamber walls (Zhang et al., 2014; Matsunaga and Ziemann, 2010).

215   Blacklights covering two of the chamber walls were then turned on for 60 min to form OH

216   radicals by methyl nitrite photolysis (Atkinson et al., 1981). The amount of n-alkane reacted

217   was measured by collecting Tenax® samples before and after the experiment and analyzing by

218   gas chromatography with flame ionization detection (GC-FID). Aerosol volume concentrations

219   were measured using a scanning mobility particle sizer (Docherty et al., 2005) and converted

220   to an SOA mass formed using a density of 1.06 g cm^{-3}. SOA mass yields (mass of SOA

221   formed/mass of n-alkane reacted) were calculated from the measured SMPS mass (corrected

222   for particle wall loss using the ~20% h^{-1} decay in mass after the lights were turned off) and the

223   GC-FID analyses. The final SOA mass concentrations were in the range of ~300 – 6000 µg m^{-}

224   ^{3} depending on precursors (Lim and Ziemann, 2009b). The SOA yields measured in these

225   experiments were reported previously (Lim and Ziemann, 2009b), but in light of a recent

226   comparison of the accuracy of our SMPS measurements with filter sampling the values reported

227   here are higher by a factor of 1.24 (Bakker-Arkema and Ziemann, 2021).

228   A temperature-programmed thermal desorption (TPTD) method was also used to

229   measure thermal desorption temperatures of DOS that was present as seed particles in n-alkane

230   SOA. Particles were sampled directly from the chamber into a thermal desorption particle beam

231   mass spectrometer (Tobias et al., 2000), where they were formed into a beam inside an

232   aerodynamic lens, transported into a high vacuum chamber, and impacted on a copper rod

233   vaporizer that was coated with a non-stick polymer and cooled to –40°C. Note that compounds

234   with vapor pressure <10^{-5} Torr is estimated to undergo negligible evaporation with the residence

235   time of ~0.2 s in the aerodynamic lens (Tobias et al., 2000). After sampling for 30 min, the

236   vaporizer was warmed by room air to –5°C and then heated at 2°C min^{-1} to 200°C. Compounds

237   desorbed according to volatility and entered a quadrupole mass spectrometer, where they were

238   ionized by 70 eV electrons prior to mass analysis. In one recent n-hexadecane experiment, the

239   composition of nitrate, hydroxyl, carbonyl (ketone + aldehyde), carboxylic acid, ester, and

240   peroxide functional groups in SOA was measured using derivatization-spectrophotometric

241   methods, with the amount of -CH$_2$- groups calculated by difference (Ranney et al., 2023). We

242   note that in that experiment the SOA yield measured by filter sampling was nearly identical to

243   the one we measured previously after applying the above correction.

244

245   **Results and discussion**

246   **SOA yields and viscosity.**

247   Figure 1 shows comparisons of measurements and modeling for (a) SOA yields, (b)

248   functional group distributions, (c) N:C ratios, and (d) O:C ratios. Figure 1(a) shows the

249   measured yields of SOA generated from the oxidation of n-alkanes (C$_n$H$_{2n+2}$; n = 8 - 17) (Lim

250   and Ziemann, 2009b). The model base case (black line) with mass accommodation coefficient

251   of 1 for all species represents no kinetic limitations in the particle phase and the results are

similar to previous simulations performed by La et al. (2016). Vapor wall loss was considered based on experimental observations and previous modeling studies (Krechmer et al., 2016; La et al., 2016; Lim and Ziemann, 2009b), which is important to account for as no wall loss would lead to a significant overestimation of SOA yields, as shown in the black dotted line and was discussed in detail in La et al. (2016). Both experimental and simulated SOA yields increase with an increase of n, reflecting the decrease in volatility of the precursor and its oxidation products (Shiraiwa et al., 2014). The observed SOA yield trend is consistent with measurements by a thermal desorption particle beam mass spectrometer, showing that n-alkane SOA are composed of less oxidized products with lower volatility for precursors with higher n (Lim and Ziemann, 2009b, a).

The overall good agreement suggests that multigenerational chemistry in the gas phase and partitioning of semi- and low-volatile products, as explicitly treated by GECKO-A box modeling, are the dominant pathway of n-alkane SOA formation under these conditions. It also suggests that peroxy radicals ($RO_2^.$) mainly react with NOx, minimizing auto-oxidation and gas-phase dimerization by $RO_2^. + RO_2^.$ reactions. Good model agreement also suggests that particle-phase oligomerization chemistry is not a dominant process, while particle-phase unimolecular reactions including cyclization of hydroxyketones and dehydration of cyclic hemiacetals forming dihydrofurans are treated in the model as they are important for the further oxidation due to the presence of a double bound in the dihydrofurans (Lim and Ziemann, 2009a; La et al., 2016). Thus, the GECKO-A model seemingly treats all essential processes for simulations of n-alkane SOA formation under high NOx conditions. Note that a very recent study suggested that cyclic hemiacetals form acetal dimers in the particle phase for SOA formed from the reaction of n-hexadecane SOA and OH/NOx (Ranney et al., 2023). In addition, particle-phase chemistry was shown to be substantial in n-alkane SOA formation under low NOx conditions through peroxyhemiacetal and oligomer formation (Shiraiwa et al., 2013; Ziemann and Atkinson, 2012). The impact of such particle-phase chemistry may warrant further investigations by future model development and experimental studies.

To explore the potential impacts of particle phase state on SOA formation and partitioning, we implemented an effective mass accommodation coefficient (α_{eff}) which can effectively consider kinetic limitations of bulk diffusion and also account for the effect of vapor pressure on partitioning kinetics for species with various volatilities (Shiraiwa and Pöschl, 2021). Bulk diffusivity evolves upon SOA formation, which can be derived by viscosity and T_g as predicted from the machine learning-based tgBoost model (dashed green line in Fig. 1a) and the compositional parametrization (CP, dashed orange line in Fig. 1a). The simulated SOA

286   yields with tgBoost are very similar to the base case scenario with $\alpha = 1$, while the application

287   of the CP leads to smaller SOA yields for $n = 15$-17. These results indicate that α_{eff} is close to

288   1 with little kinetic limitations of bulk diffusion for most cases, except some limitations are

289   predicted by CP for large precursors. Deviations of tgBoost and CP stem from the difference in

290   phase state and viscosity predicted by the two methods.

291   Figure 2(a) shows the simulated viscosity and corresponding bulk diffusivity of n-

292   alkane SOA. Remarkably, the two models predict contrasting trends. The simulated glass

293   transition temperature ($T_{g,org}$) of SOA is presented in Fig. A1. The CP predicts a decrease in

294      $T_{g,org}$ for $C_{8\text{-}12}$ with the lowest $T_{g,org}$ of ~250 K, which is likely due to a decrease of O:C ratio

295   (Fig. 1d) as lower O:C ratio can lead to a decrease of T_g (DeRieux et al., 2018; Shiraiwa et al.,

296   2017), followed by an increase of $T_{g,org}$ with n to reach ~270 K with C_{17}. These values

297   correspond to viscosity of 10^4 - 10^6 Pa s, indicating that n-alkane SOA adopts viscous semisolid

298   phase state. The increase of viscosity for larger precursors is apparently reasonable, as their

299   oxidation products would have higher molar mass which would generally correspond to higher

300      $T_{g,org}$ (Koop et al., 2011; Shiraiwa et al., 2017). Based on the Stokes-Einstein relation, bulk

301   diffusivity would be in the range of 3×10^{-15} - 10^{-12} cm^2 s^{-1}. The characteristic timescale of bulk

302   diffusion in an average particle diameter of 300 nm can be as low as ~2 hours (Shiraiwa et al.,

303   2011), which is longer than experimental timescale of one hour. These low diffusivities and

304   long diffusion timescale can induce concentration gradients in the particle bulk, reducing α_{eff}

305   to cause significant kinetic limitations to retard SOA growth, which is not consistent with the

306   measured SOA yields.

307   tgBoost predicts the opposite trend, predicting a monotonic decrease of $T_{g,org}$ and

308   viscosity with an increase of n, suggesting that SOA phase state shifts from an amorphous

309   semisolid state ($10^2 < \eta < 10^5$ Pa s) towards a liquid-like phase state ($\eta < 10^2$ Pa s). These

310   results are counter-intuitive as T_g values of n-alkanes increases with an increase of n, which can

311   be reproduced with great precision by tgBoost (Galeazzo and Shiraiwa, 2022). The

312   determinants explaining this unexpected trend are chemical composition and molecular

313   structure of the oxidation products as discussed below. The characteristic timescale of bulk

314   diffusion is less than one second in a low viscous state and high bulk diffusivity (Shiraiwa et

315   al., 2011) and SOA particles are expected be homogeneously well-mixed. Hence, α_{eff} remains

316   very close to 1 with little kinetic limitation of bulk diffusion.

317   Unfortunately, no direct viscosity measurements of n-alkane SOA generated under high

318   NO$_x$ conditions are available to date, while there are two studies for n-alkane SOA generated

319   under NOx-free conditions. Saukko et al. (2012) (Saukko et al., 2012) observed that n-
320   heptadecane ($C_{17}H_{36}$) SOA with low O:C ratio did not bounce from an impactor plate. It
321   indicates that these particles adopted a liquid-like state, as indicated by the violet shading in
322   Fig. 2(a), which is consistent with the tgBoost prediction. Shiraiwa et al. (2013) estimated bulk
323   diffusivity of n-dodecane ($C_{12}H_{26}$) SOA generated without NO_x to be 10^{-12} cm^2 s^{-1} using a
324   kinetic multilayer model to simulate evolution of particle size distribution. While these two data
325   points cannot be directly compared with the viscosity predictions of high NOx n-alkane SOA,
326   they serve as reference data points for now and direct viscosity or bulk diffusivity
327   measurements of high NO_x n-alkane SOA are warranted in future studies.

328   Figure 2(b) shows the thermal desorption profiles of DOS that was present as seed
329   particles within the SOA formed from oxidation of the n-alkanes. Since DOS desorption
330   involved diffusion through the SOA prior to escape into vacuum, these profiles provided a
331   means for probing the SOA viscosity. The peaks in the DOS profiles for the C_{8-13} and C_{14-17} n-
332   alkanes are closely grouped, with vaporizer temperature at ~80 °C and ~65 °C, respectively,
333   with the peak for pure DOS occurring in between at ~72°C. The observed decrease in desorption
334   temperatures from low to high carbon numbers suggests an increase in effective volatility of
335   DOS in SOA generated from larger n-alkanes. In addition, Lim and Ziemann (2009) have
336   observed that C_{10} n-alkane SOA generated under high NOx conditions evaporate at higher
337   temperatures compared to C_{12} and C_{15} n-alkane SOA based on total ion thermal desorption
338   measurements (Lim and Ziemann, 2009b). Volatility and T_g were shown to exhibit clear
339   anticorrelation (Li et al., 2020); hence, these results strongly indicate that C_{8-13} SOA have higher
340   T_g and viscosity compared to C_{13-17} SOA. It is remarkable to note that the C_{13} profile is bimodal
341   with peaks at ~80 °C and ~65 °C (Fig. 2b), which is in line with tgBoost prediction that the
342   viscosity of C_{13} alkane SOA is at the edge of amorphous semi-solid and liquid phase states (Fig.
343   2a). These results indicate that n-alkane SOA generated by larger precursors adopt low viscous
344   liquid-like states, while n-alkane SOA generated by smaller precursors adopt viscous semisolid
345   states, in agreement with tgBoost predictions. The major strength of tgBoost is that it considers
346   molecular structure and functionality for T_g predictions, while the compositional
347   parameterization does not account for this effect, leading to intuitive but erroneous predictions.
348

Chemical composition of SOA.

350   Figure 1 also shows the simulated (c) N:C and (d) O:C ratios of SOA with $\alpha = 1$ (black
351   line) and $\alpha = \alpha_{eff}$ with T_g determined with tgBoost (green line) or the compositional

parameterization (orange line). The N:C ratio is very similar among all simulations being ~0.2 for C_8 and decreasing progressively to ~0.03 with each addition of a carbon atom in the precursor. O:C ratios were calculated in two different ways by treating a nitrate ($-ONO_2$) group to contain either three (solid lines) or one (dashed lines) oxygen atoms. One oxygen atom is also considered because O:C ratios reported from aerosol mass spectrometer measurements generally treat a nitrate group the same as a hydroxyl group, since they have the same effect on oxidation state (Farmer et al., 2010). Similar to the N:C ratio, there is a constant decrease in O:C of SOA with increasing n, which is consistent with previous measurements for n-pentadecane ($C_{15}H_{32}$) SOA (Aimanant and Ziemann, 2013a) and n-hexadecane ($C_{16}H_{34}$) SOA in this study, even though the simulated values are ~45% and 15% lower than the measured N:C and O:C ratios, respectively. The discrepancies are likely due to errors on modeling gas-wall partitioning and gas-particle partitioning. The difference may also be caused by missing processes in the model such as reactive uptake of oxidants and particle-phase chemistry.

We measured functional group distributions in n-hexadecane SOA using derivatization-spectrophotometric methods described in Aimanant and Ziemann (2013b), as shown in Fig. 1(b) and summarized in Table A1. Experimental measurements report high presence of $-CH_2-$ (13.81) and $-ONO_2$ (0.91), followed by ROH (0.41), RC(=O) (0.38), and RC(=O)OR (0.28), with the average measured number of groups per C_{16} molecule in parenthesis. Figure 1(b) includes simulation results by GECKO-A with CP and tgBoost, showing overall satisfactory agreement. The simulated results with tgBoost show excellent agreement for hydroxyl and methylene groups, while the simulated nitrates and carbonyls (ketones + aldehydes) are lower than the measurements. The simulation by CP has also a similar trend, but with significantly lower presence of nitrates, carbonyls, and esters.

Figure 3(a) shows the top 15 oxidation products in the particle phase formed by the oxidation of n-hexadecane simulated by GECKO-A box model with tgBoost. Note that positional isomers are lumped into one species and that the five species in the first row constitute majority (~86%) of SOA mass. The simulated SOA is composed mostly by 1st generation products including alkyl nitrates, hydroxynitrates, and hydroxyketones. There is also a significant presence of 2nd and 3rd generation products such as esters and dinitrates. We also found multi-functionalized decomposition products including smaller chain hydroxy nitrates and alkyl lactones as well as particle-phase products from cyclization of hydroxyketones and dehydration of cyclic hemiacetals to form dihydrofurans. A very recent study by Ranney et al. (2023) measured n-hexadecane oxidation products under high NOx, finding that alkyl nitrates, hydroxyl nitrates, hydroxyl carbonyls, cyclic hemiacetals, and cyclic hemiacetal nitrates are

major products. These compounds are indeed major products as shown in Fig. 3a, confirming that GECKO-A simulated n-alkane oxidation very well. There are notable differences in molecular composition for SOA simulated by CP (Fig. A2): the major compounds are 1st generation single and multi-functionalized products, followed by some 2nd and 3rd generation products, without decomposition products in the top species.

The simulated T_g by both methods for each compound are listed in Fig. 3. Overall tgBoost predicts T_g to be 157 – 221 K which are much lower compared to CP, especially with significant differences for organic nitrates and multi-functionalized species. As tgBoost considers the molecular structure, functional group and atomic interconnectivity of a molecule, it should make better predictions for multi-functionalized compounds based on the presence of different functional groups. CP is based on elemental composition and it predicts high T_g for compounds with high molar mass, predicting same T_g for isomers. In addition, the CP for CHON compounds was developed based on T_g values mainly estimated from their melting points, as there are limited number of CHON compounds with measured T_g available. T_g of organic nitrates are especially scarce and future T_g measurements for organic nitrates are desired to improve T_g parameterizations. For these reasons, CP overestimates T_g for oxidation products of n-alkane with long chain on average by ~66 K compared to tgBoost, overpredicting SOA viscosity as shown in Fig. 2(a).

Figure 3 also lists α_{eff} values, showing that they are very close to 1 for tgBoost, with SOA to be low viscous liquid with little kinetic limitations in mass accommodation. Additional oxidation products with lower concentrations are listed in Fig. A3 and their α_{eff} remain also close to 1. In contrast, as CP predicts the SOA phase state to be viscous amorphous semisolid, α_{eff} values for semi-volatile compounds become significantly smaller to kinetically limit mass accommodation. This decrease of α_{eff} is larger for compounds with higher volatility, as such compounds have higher re-evaporation rate on viscous particles with lower rate of bulk diffusion (Shiraiwa and Pöschl, 2021) (Fig. A3). α_{eff} for lower volatility compounds remain high, as they exhibit much lower desorption rates and are less likely to re-evaporate, even if their diffusion into the bulk is slow. Consequently, SOA simulated with CP mainly consists of later generation products with higher functionalization and molar masses.

Figure 3(b) shows top 15 oxidation products of n-decane ($C_{10}H_{26}$) as predicted by GECKO-A with tgBoost. SOA is mostly composed of 2nd and 3rd generation products with multiple functional groups including nitrates, ketones, and alcohols. These highly oxidized products have T_g in the range of 225 – 304 K, with similar predictions by CP and tgBoost. This

419   is consistent with previous studies that demonstrated successful applications of CP to predict

420   the measured viscosity of SOA derived from biogenic and other relatively small precursors

421   (DeRieux et al., 2018; Smith et al., 2021; Baboomian et al., 2022). These results are consistent

422   with total ion thermal desorption profiles of n-alkane SOA formed in the presence of NOx (Lim

423   and Ziemann, 2009b): C_{10} SOA was observed to have a broad single peak around ~75 °C,

424   indicating the presence of low volatility multigenerational products; in contrast, C_{12} and C_{15}

425   SOA exhibited two peaks with one larger peak at lower temperature, corresponding to 1st

426   generation products and another smaller peak for multigenerational products. The phase state

427   of n-decane SOA is predicted to be semisolid, but kinetic limitations are not strong as α_{eff} values

428   for most compounds are only slightly reduced from 1.

429

430   **Effects of mass loadings on viscosity.**

431   The use of higher mass loadings in chamber experiments than ambient conditions

432   assured that the condensation of semi-volatile vapors to suspended particles is a dominant

433   process over vapor wall deposition (Zhang et al., 2014; Matsunaga and Ziemann, 2010).

434   Chamber experiments of n-alkane photooxidation at high NO_x were also conducted with lower

435   mass loading by Presto et al. (2010), who measured temporal evolution of SOA yields as shown

436   in Fig. 4(a). SOA yields are increased with an increase of SOA mass concentrations, which is

437   consistent with SOA absorptive partitioning theory (Pankow, 1994). The oxidation of larger

438   precursors leads to higher SOA yields, in agreement with Lim and Ziemann (2009b) as

439   presented in Fig. 1a. As shown with solid lines, the GECKO-A box model simulated

440   experimental observations of SOA yields very well.

441   Figure 4(b) depicts the simulated SOA viscosity. We observed the same trend as Fig.

442   2(a) with lowering of viscosity upon an increase of carbon number n. SOA phase state is

443   predicted to be semisolid for low carbon n, while it is expected to be liquid for high n. The

444   predicted viscosity is about one order of magnitude higher compared to Fig. 2(a). Lower mass

445   loadings suppress partitioning of higher volatility compounds, resulting in higher viscosity as

446   condensation would be dominated by lower volatility compounds with higher T_g (Jain et al.,

447   2018; Champion et al., 2019; Grayson et al., 2016; DeRieux et al., 2018).

448

449   **Atmospheric Implications.**

450   The phase state and viscosity of SOA formed by IVOCs have been largely unknown

451   and unexplored. We demonstrated in this study that SOA derived from small and middle size

452   n-alkane (C_{12} and smaller) mostly consists of multigenerational oxidation products to adopt an

amorphous semisolid state, while larger n-alkane SOA are mainly composed of first generation lightly oxidized products to adopt a low viscous liquid state. This result is counter-intuitive, as it has been established that higher molar mass would lead to higher glass transition temperature, and hence, higher viscosity (Koop et al., 2011; Shiraiwa et al., 2017). In fact, the viscosity of biogenic SOA follows this trend: the viscosity of isoprene (C_5H_8) SOA is reported to be lower than monoterpene ($C_{10}H_{16}$, such as α-pinene and limonene) SOA (Renbaum-Wolff et al., 2013; Zhang et al., 2019), while oxidation products of sesquiterpene ($C_{15}H_{24}$) increase viscosity of SOA (Smith et al., 2021), which is captured by empirical parameterizations based on elemental composition (DeRieux et al., 2018; Li et al., 2020). In contrast, n-alkane SOA exhibits an opposite trend, as indicated by thermal desorption measurements that show that DOS in SOA formed by oxidation of large n-alkanes has higher volatility. Hence, the SOA has lower viscosity, due to the enhanced presence of less functionalized first-generation products (Li et al., 2020; Zhang et al., 2019). This trend is successfully predicted by GECKO-A combined with machine learning-based model tgBoost, which emphasizes the importance of consideration of functionality and molecular structure in accurate predictions of T_g. The relationship between viscosity and composition is also reflected in the atomic O:C and N:C ratios of n-alkane SOA, which decrease monotonically upon an increase of carbon number of the n-alkane, since higher oxidation state and functionalization can increase T_g (DeRieux et al., 2018; Koop et al., 2011; Shiraiwa et al., 2017; Saukko et al., 2012).

IVOCs have gained growing attention for better characterization of urban air quality, as they represent an important source of SOA as shown by chamber experiments (Aimanant and Ziemann, 2013a; Lim and Ziemann, 2009b) and as observed in field observations (Gentner et al., 2012; Li et al., 2022; Robinson et al., 2007; McDonald et al., 2018). While a few large-scale aerosol models treat IVOC SOA to achieve better agreement with ambient measurements (de Gouw et al., 2011; Li et al., 2022; Zhao et al., 2016), IVOC SOA is still highly uncertain in terms of chemical composition and particle phase state and model parameters and treatments for SOA formation and partitioning are poorly constrained. Our study provides critical insights for these aspects, showing that n-alkane SOA formation under high NOx conditions (as usually the case for ambient urban air) is dominated by gas-phase chemistry followed by partitioning. As the generated SOA particles adopt a low viscous state, there is little kinetic limitations of mass accommodation and bulk diffusion, which supports the application of equilibrium SOA partitioning in the boundary layer. While the experiments and modeling were conducted for dry conditions in this study, the phase state and viscosity of ambient n-alkane SOA would be expected to be even lower under humid conditions due to hygroscopic growth and water acting

as plasticizer. Note that further experiments and model simulations are required for different conditions for middle and upper free troposphere, as viscosity is expected to become higher under low temperatures.

It is highly remarkable that the combination of tgBoost and GECKO-A box model accurately simulates SOA yields, functional group distributions and phase state. This new model represents a unique and comprehensive tool for simulating formation, partitioning and chemical evolution of SOA, opening up a new avenue for analyzing complex interplay of gas-phase chemistry and particle-phase processes and composition in SOA for detailed analysis and interpretation of laboratory experiments and field observations. In addition, we propose to pursue the application of this model as a basis for the development of a detailed master mechanism of multiphase aerosol chemistry as well as for the derivation of simplified but realistic parameterizations for air quality and climate models. In regional and global air quality models, it is challenging and computationally very expensive to treat complex SOA multiphase processes. Thus, such processes should be treated in efficient but effective way and the new model shall serve as benchmark for the development of simplified SOA descriptions.

Acknowledgements. This work was also funded by U.S. Department of Energy (DE-SC0018349), U.S. National Science Foundation (AGS-1654104) and the Campus France (Make Our Planet Great Again short stay program grant, mopga-short-0000000116). In addition, PZ acknowledges support from the National Science Foundation under grant AGS-1750447.

Authors contributions. TG and MS designed the study. TG conducted model simulations and data analysis. RV, MC, and BA developed the GECKO-A model. YL and PZ conducted experimental measurements. All authors discussed the results. TG and MS wrote the manuscript with contributions from all coauthors.

Competing interests. At least one of the (co-)authors is a member of the editorial board of Atmospheric Chemistry and Physics.

Code/Data availability. The simulation data may be obtained from the corresponding author upon request. The model tgBoost is available in Github (https://github.com/U0M0Z/tgpipe) and in the homepage (https://azothai.ps.uci.edu/).

520
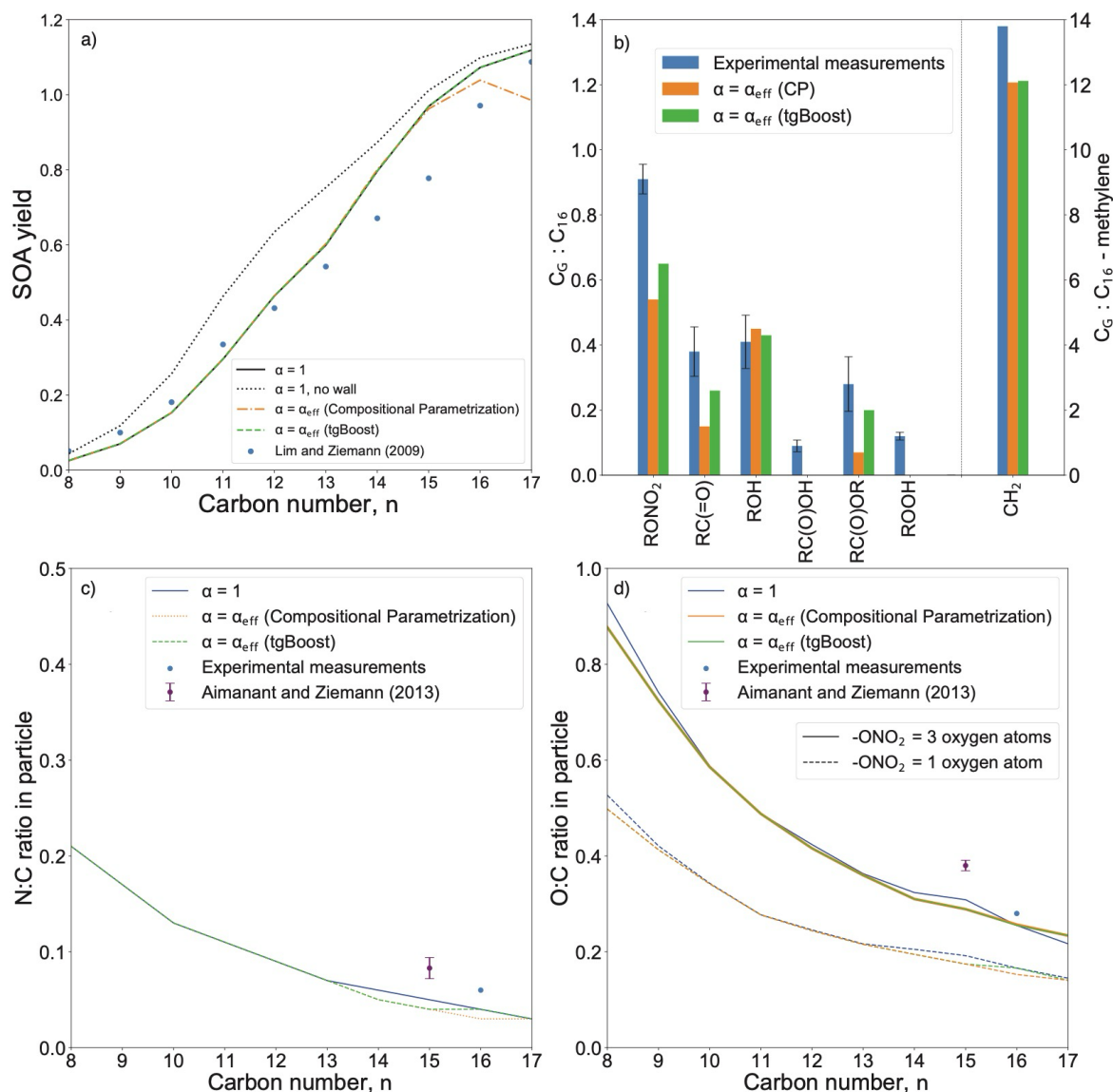
Figure 1: (a) Yields of SOA generated from OH oxidation of linear n-alkanes as measured by Lim and Ziemann (2009) (markers) (Lim and Ziemann, 2009b) and modeled by the GECKO-A box model (lines). The black line represents the base case with mass accommodation coefficient (α) of 1. The dashed lines represent simulations with effective mass accommodation coefficient (α_{eff}) as a function of bulk diffusivity from tgBoost (green) and the compositional parameterization (orange). (b) Simulated functional group distributions of n-hexadecane ($C_{16}H_{34}$) oxidation products in the particle phase. The blue bars represent experimental measurements. The green and orange bars represent GECKO-A box model simulations with α_{eff} with tgBoost and the compositional parameterization, respectively. (c) N:C and (d) O:C ratios in SOA formed by n-alkane oxidation simulated by the GECKO-A box model. The black line represents the base case with α of 1. The dashed lines represent simulations with α_{eff} with tgBoost (green) and the compositional parameterization (orange).

533
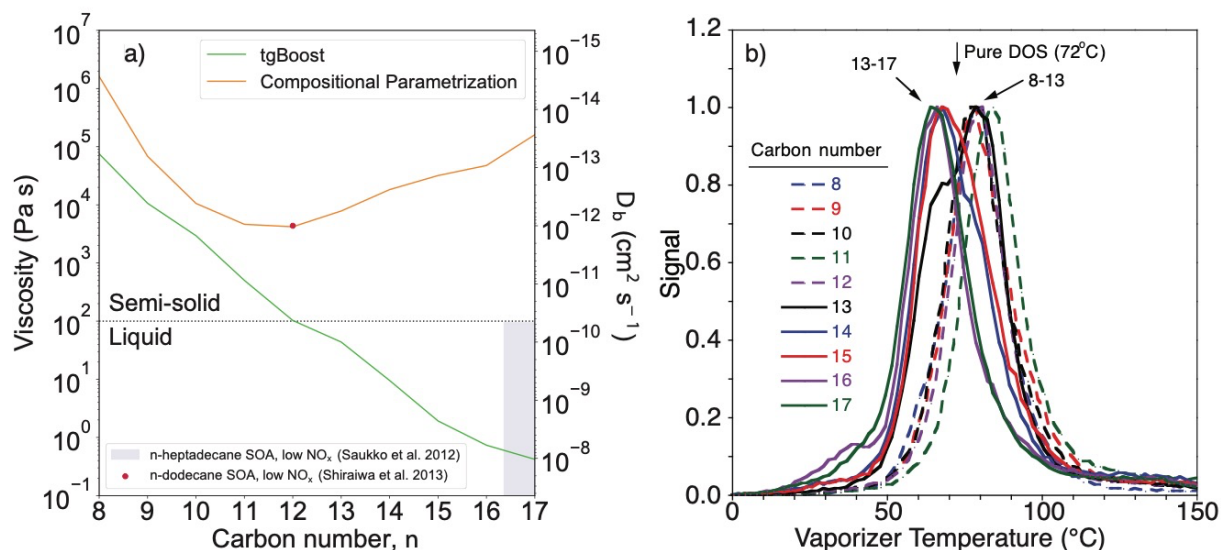
Figure 2: Phase state of n-alkane SOA. (a) Predicted viscosity of SOA generated from n-alkanes as computed by the GECKO-A box model with the T_g compositional parametrization (orange line) and tgBoost (green line) at the last step of the simulations (t = 3600 s). (b) Thermal desorption temperatures of dioctyl sebacate (DOS) that was present as seed particles in n-alkane SOA.
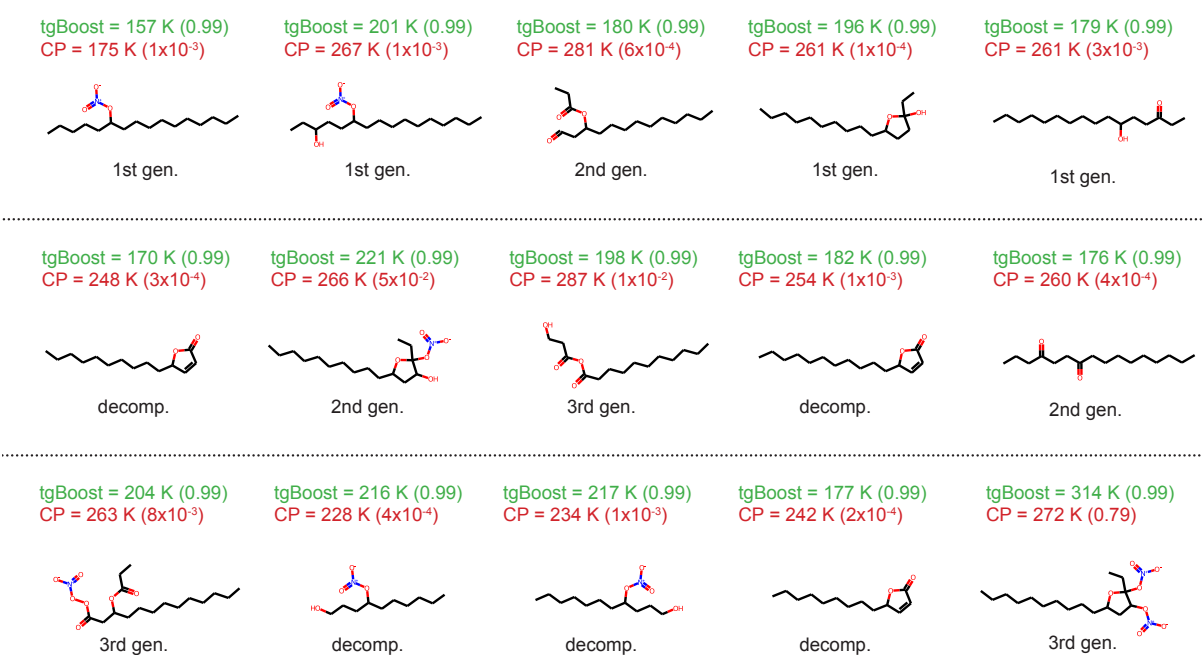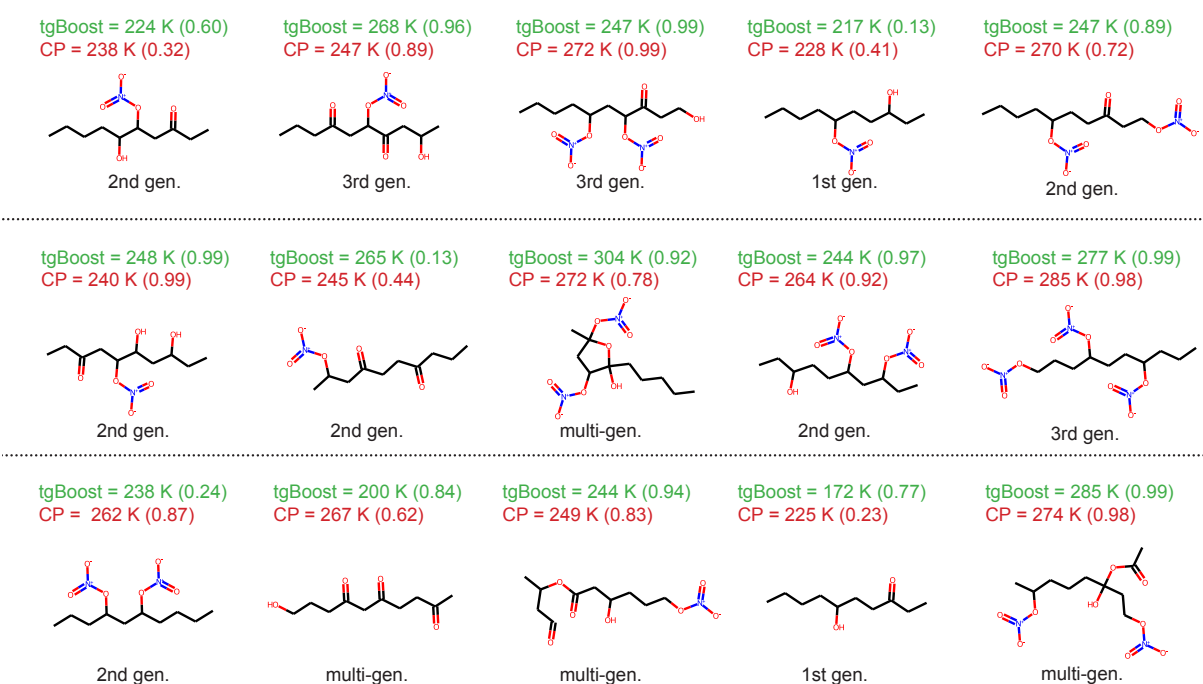
539
540 **Figure 3:** Molecular composition of oxidation products of n-alkanes under high NOx
541 conditions in the particle phase. Top 15 SOA contributors with highest concentrations in (a) n-
542 Hexadecane ($C_{16}H_{34}$) SOA and (b) n-Decane ($C_{10}H_{32}$) simulated by GECKO-A with effective
543 mass accommodation coefficient (α_{eff}) with tgBoost. The species are reported in descending
544 concentrations from left to right and from top to bottom. Positional isomers are lumped into
545 one species. Listed values are T_g as calculated by tgBoost and CP and α_{eff} values at the end of
546 simulation (3600 s) in brackets. Types of compounds are also noted (1st, 2nd, and 3rd generation
547 products, decomposition products).
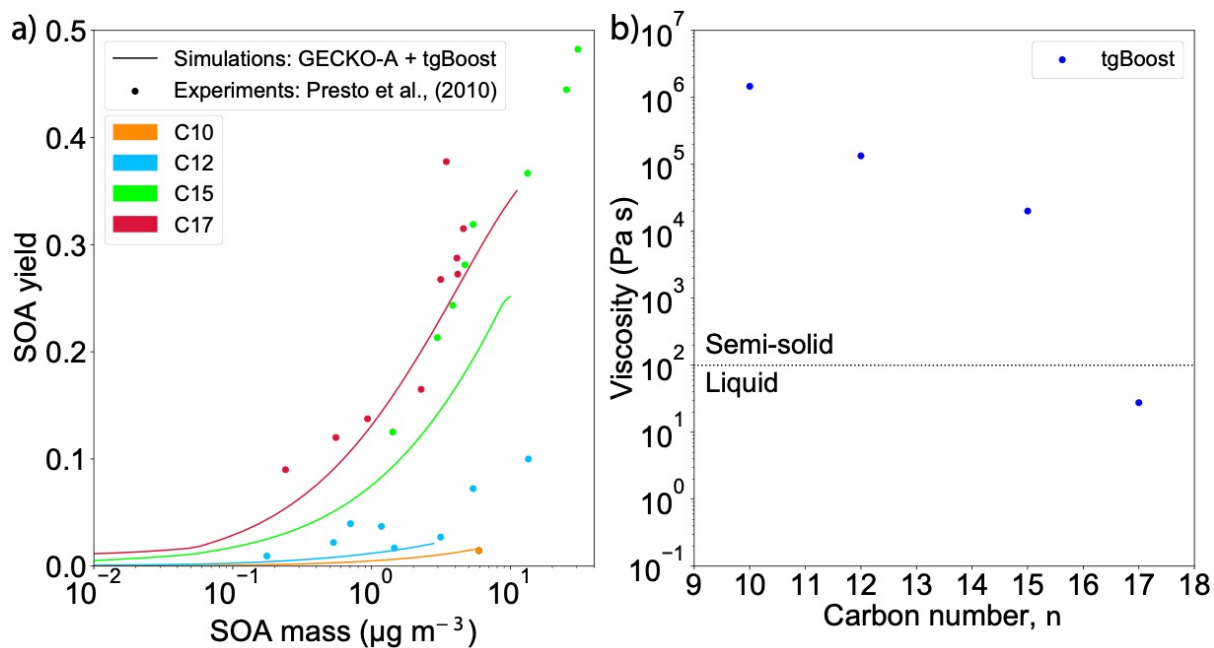
548
549
550 **Figure 4:** Effects of mass loadings on SOA yields and viscosity. (a) SOA yields from photo-
551 oxidation of n-decane (C10), n-dodecane (C12), n-pentadecane (C15), and n-heptadecane
552 (C17) at high NOx as a function of SOA mass concentration, as measured in Presto et al. (2010)
553 (markers) and as modeled by the GECKO-A box model combined with tgBoost (lines). (b)
554 SOA viscosity as modeled by the GECKO-A box model combined with tgBoost.
555

References.

Aimanant, S. and Ziemann, P. J.: Chemical Mechanisms of Aging of Aerosol Formed from the Reaction of n-Pentadecane with OH Radicals in the Presence of NOx, Aerosol Sci. Technol., 47, 979-990, 10.1080/02786826.2013.804621, 2013a.

Aimanant, S. and Ziemann, P. J.: Development of Spectrophotometric Methods for the Analysis of Functional Groups in Oxidized Organic Aerosol, Aerosol Sci. Technol., 47, 581-591, 10.1080/02786826.2013.773579, 2013b.

Atkinson, R., Carter, W. P. L., Winer, A. M., and Pitts, J. N.: An Experimental Protocol for the Determination of OH Radical Rate Constants with Organics Using Methyl Nitrite Photolysis as an OH Radical Source, Journal of the Air Pollution Control Association, 31, 1090-1092, 10.1080/00022470.1981.10465331, 1981.

Aumont, B., Szopa, S., and Madronich, S.: Modelling the evolution of organic carbon during its gas-phase tropospheric oxidation: development of an explicit model based on a self generating approach, Atmospheric Chemistry and Physics, 5, 2497-2517, 10.5194/acp-5-2497-2005, 2005.

Aumont, B., Valorso, R., Mouchel-Vallon, C., Camredon, M., Lee-Taylor, J., and Madronich, S.: Modeling SOA formation from the oxidation of intermediate volatility n-alkanes, Atmospheric Chemistry and Physics, 12, 7577-7589, 10.5194/acp-12-7577-2012, 2012.

Aumont, B., Camredon, M., Mouchel-Vallon, C., La, S., Ouzebidour, F., Valorso, R., Lee-Taylor, J., and Madronich, S.: Modeling the influence of alkane molecular structure on secondary organic aerosol formation, Faraday Discussions, 165, 105-122, 10.1039/C3FD00029J, 2013.

Baboomian, V. J., Crescenzo, G. V., Huang, Y., Mahrt, F., Shiraiwa, M., Bertram, A. K., and Nizkorodov, S. A.: Sunlight can convert atmospheric aerosols into a glassy solid state and modify their environmental impacts, Proc. Nat. Acad. Sci., 119, e2208121119, 10.1073/pnas.2208121119, 2022.

Bakker-Arkema, J. G. and Ziemann, P. J.: Minimizing Errors in Measured Yields of Particle-Phase Products Formed in Environmental Chamber Reactions: Revisiting the Yields of β-Hydroxynitrates Formed from 1-Alkene + OH/NOx Reactions, ACS Earth and Space Chemistry, 5, 690-702, 10.1021/acsearthspacechem.1c00008, 2021.

Champion, W. M., Rothfuss, N. E., Petters, M. D., and Grieshop, A. P.: Volatility and Viscosity Are Correlated in Terpene Secondary Organic Aerosol Formed in a Flow Reactor, Environmental Science & Technology Letters, 6, 513-519, 10.1021/acs.estlett.9b00412, 2019.

de Gouw, J. A., Middlebrook, A. M., Warneke, C., Ahmadov, R., Atlas, E. L., Bahreini, R., Blake, D. R., Brock, C. A., Brioude, J., Fahey, D. W., Fehsenfeld, F. C., Holloway, J. S., Le Henaff, M., Lueb, R. A., McKeen, S. A., Meagher, J. F., Murphy, D. M., Paris, C., Parrish, D. D., Perring, A. E., Pollack, I. B., Ravishankara, A. R., Robinson, A. L., Ryerson, T. B., Schwarz, J. P., Spackman, J. R., Srinivasan, A., and Watts, L. A.: Organic Aerosol Formation Downwind from the Deepwater Horizon Oil Spill, Science, 331, 1295-1299, 10.1126/science.1200320, 2011.

596 DeRieux, W. S. W., Li, Y., Lin, P., Laskin, J., Laskin, A., Bertram, A. K., Nizkorodov, S. A.,
597 and Shiraiwa, M.: Predicting the glass transition temperature and viscosity of secondary organic
598 material using molecular composition, Atmos. Chem. Phys., 18, 6331-6351, 10.5194/acp-18-
599 6331-2018, 2018.

600 Dette, H. P., Qi, M., Schröder, D. C., Godt, A., and Koop, T.: Glass-forming properties of 3-
601 Methylbutane-1,2,3-tricarboxylic acid and its mixtures with water and pinonic acid, The
602 Journal of Physical Chemistry A, 118, 7024-7033, 10.1021/jp505910w, 2014.

603 Docherty, K. S., Wu, W., Lim, Y. B., and Ziemann, P. J.: Contributions of organic peroxides
604 to secondary aerosol formed from reactions of monoterpenes with O_3, Environ. Sci. Technol.,
605 39, 4049-4059, 10.1021/es050228s, 2005.

606 Evoy, E., Maclean, A. M., Rovelli, G., Li, Y., Tsimpidi, A. P., Karydis, V. A., Kamal, S.,
607 Lelieveld, J., Shiraiwa, M., Reid, J. P., and Bertram, A. K.: Predictions of diffusion rates of
608 large organic molecules in secondary organic aerosols using the Stokes–Einstein and fractional
609 Stokes–Einstein relations, Atmos. Chem. Phys., 19, 10073-10085, 10.5194/acp-19-10073-
610 2019, 2019.

611 Farmer, D. K., Matsunaga, A., Docherty, K. S., Surratt, J. D., Seinfeld, J. H., Ziemann, P. J.,
612 and Jimenez, J. L.: Response of an aerosol mass spectrometer to organonitrates and
613 organosulfates and implications for atmospheric chemistry, Proc. Nat. Acad. Sci., 107, 6670-
614 6675, 2010.

615 Galeazzo, T. and Shiraiwa, M.: Predicting glass transition temperature and melting point of
616 organic compounds via machine learning and molecular embeddings, Environmental Science:
617 Atmospheres, 2, 362-374, 10.1039/D1EA00090J, 2022.

618 Galeazzo, T., Valorso, R., Li, Y., Camredon, M., Aumont, B., and Shiraiwa, M.: Estimation of
619 secondary organic aerosol viscosity from explicit modeling of gas-phase oxidation of isoprene
620 and α-pinene, Atmos. Chem. Phys., 21, 10199-10213, 10.5194/acp-21-10199-2021, 2021.

621 Gentner, D. R., Isaacman, G., Worton, D. R., Chan, A. W. H., Dallmann, T. R., Davis, L., Liu,
622 S., Day, D. A., Russell, L. M., Wilson, K. R., Weber, R., Guha, A., Harley, R. A., and Goldstein,
623 A. H.: Elucidating secondary organic aerosol from diesel and gasoline vehicles through detailed
624 characterization of organic carbon emissions, Proc. Nat. Acad. Sci., 109, 18318-18323,
625 10.1073/pnas.1212272109, 2012.

626 Grayson, J. W., Zhang, Y., Mutzel, A., Renbaum-Wolff, L., Böge, O., Kamal, S., Herrmann,
627 H., Martin, S. T., and Bertram, A. K.: Effect of varying experimental conditions on the viscosity
628 of α-pinene derived secondary organic material, Atmos. Chem. Phys., 16, 6027-6040,
629 10.5194/acp-16-6027-2016, 2016.

630 Grayson, J. W., Evoy, E., Song, M., Chu, Y., Maclean, A., Nguyen, A., Upshur, M. A.,
631 Ebrahimi, M., Chan, C. K., Geiger, F. M., Thomson, R. J., and Bertram, A. K.: The effect of
632 hydroxyl functional groups and molar mass on the viscosity of non-crystalline organic and
633 organic–water particles, Atmos. Chem. Phys., 17, 8509-8524, 10.5194/acp-17-8509-2017,
634 2017.

635 Jain, S., Fischer, B. K., and Petrucci, A. G.: The Influence of Absolute Mass Loading of
636 Secondary Organic Aerosols on Their Phase State, Atmosphere, 9, 10.3390/atmos9040131,
637 2018.

638 Jenkin, M. E., Valorso, R., Aumont, B., and Rickard, A. R.: Estimation of rate coefficients and
639 branching ratios for reactions of organic peroxy radicals for use in automated mechanism
640 construction, Atmos. Chem. Phys., 19, 7691-7717, 10.5194/acp-19-7691-2019, 2019.

641 Jenkin, M. E., Valorso, R., Aumont, B., Rickard, A. R., and Wallington, T. J.: Estimation of
642 rate coefficients and branching ratios for gas-phase reactions of OH with aliphatic organic
643 compounds for use in automated mechanism construction, Atmos. Chem. Phys., 18, 9297-9328,
644 10.5194/acp-18-9297-2018, 2018a.

645 Jenkin, M. E., Valorso, R., Aumont, B., Rickard, A. R., and Wallington, T. J.: Estimation of
646 rate coefficients and branching ratios for gas-phase reactions of OH with aromatic organic
647 compounds for use in automated mechanism construction, Atmos. Chem. Phys., 18, 9329-9349,
648 10.5194/acp-18-9329-2018, 2018b.

649 Jimenez, J. L., Canagaratna, M. R., Donahue, N. M., Prevot, A. S. H., Zhang, Q., Kroll, J. H.,
650 DeCarlo, P. F., Allan, J. D., Coe, H., Ng, N. L., Aiken, A. C., Docherty, K. S., Ulbrich, I. M.,
651 Grieshop, A. P., Robinson, A. L., Duplissy, J., Smith, J. D., Wilson, K. R., Lanz, V. A., Hueglin,
652 C., Sun, Y. L., Tian, J., Laaksonen, A., Raatikainen, T., Rautiainen, J., Vaattovaara, P., Ehn,
653 M., Kulmala, M., Tomlinson, J. M., Collins, D. R., Cubison, M. J., Dunlea, E. J., Huffman, J.
654 A., Onasch, T. B., Alfarra, M. R., Williams, P. I., Bower, K., Kondo, Y., Schneider, J.,
655 Drewnick, F., Borrmann, S., Weimer, S., Demerjian, K., Salcedo, D., Cottrell, L., Griffin, R.,
656 Takami, A., Miyoshi, T., Hatakeyama, S., Shimono, A., Sun, J. Y., Zhang, Y. M., Dzepina, K.,
657 Kimmel, J. R., Sueper, D., Jayne, J. T., Herndon, S. C., Trimborn, A. M., Williams, L. R.,
658 Wood, E. C., Middlebrook, A. M., Kolb, C. E., Baltensperger, U., and Worsnop, D. R.:
659 Evolution of organic aerosols in the atmosphere, Science, 326, 1525-1529,
660 10.1126/science.1180353, 2009.

661 Julin, J., Winkler, P. M., Donahue, N. M., Wagner, P. E., and Riipinen, I. A.: Near unity mass
662 accommodation coefficient of organic molecules of varying structure, Environ. Sci. Technol.,
663 48, 12083–12089, 10.1021/es501816h, 2014.

664 Knopf, D. A. and Alpert, P. A.: Atmospheric ice nucleation, Nat. Rev. Phys., 5, 203-217,
665 10.1038/s42254-023-00570-7, 2023.

666 Koop, T., Bookhold, J., Shiraiwa, M., and Pöschl, U.: Glass transition and phase state of organic
667 compounds: dependency on molecular properties and implications for secondary organic
668 aerosols in the atmosphere, Physical Chemistry Chemical Physics, 13, 19238-19255, 2011.

669 Krechmer, J. E., Pagonis, D., Ziemann, P. J., and Jimenez, J. L.: Quantification of gas-wall
670 partitioning in Teflon environmental chambers using rapid bursts of low-volatility oxidized
671 species generated in situ, Environ. Sci. Technol., 50, 5757-5765, 2016.

672 Kroll, J. H. and Seinfeld, J. H.: Chemistry of secondary organic aerosol: Formation and
673 evolution of low-volatility organics in the atmosphere, Atmos. Environ., 42, 3593-3624,
674 10.1016/j.atmosenv.2008.01.003, 2008.

675 La, Y. S., Camredon, M., Ziemann, P. J., Valorso, R., Matsunaga, A., Lannuque, V., Lee-
676 Taylor, J., Hodzic, A., Madronich, S., and Aumont, B.: Impact of chamber wall loss of gaseous
677 organic compounds on secondary organic aerosol formation: explicit modeling of SOA
678 formation from alkane and alkene oxidation, Atmospheric Chemistry and Physics, 16, 1417-
679 1431, 10.5194/acp-16-1417-2016, 2016.

Li, J. L., Li, K., Li, H., Wang, X. Z., Wang, W. G., Wang, K., and Ge, M. F.: Long-chain alkanes in the atmosphere: A review *, J. Environ. Sci., 114, 37-52, 10.1016/j.jes.2021.07.021, 2022.

Li, Y., Day, D. A., Stark, H., Jimenez, J. L., and Shiraiwa, M.: Predictions of the glass transition temperature and viscosity of organic aerosols from volatility distributions, Atmos. Chem. Phys., 20, 8103-8122, 10.5194/acp-20-8103-2020, 2020.

Lim, Y. B. and Ziemann, P. J.: Chemistry of Secondary Organic Aerosol Formation from OH Radical-Initiated Reactions of Linear, Branched, and Cyclic Alkanes in the Presence of NOx, Aerosol Sci. Technol., 43, 604-619, 10.1080/02786820902802567, 2009a.

Lim, Y. B. and Ziemann, P. J.: Effects of Molecular Structure on Aerosol Yields from OH Radical-Initiated Reactions of Linear, Branched, and Cyclic Alkanes in the Presence of NOx, Environ. Sci. Technol., 43, 2328-2334, 10.1021/es803389s, 2009b.

Maclean, A. M., Smith, N. R., Li, Y., Huang, Y., Hettiyadura, A. P. S., Crescenzo, G. V., Shiraiwa, M., Laskin, A., Nizkorodov, S. A., and Bertram, A. K.: Humidity-Dependent Viscosity of Secondary Organic Aerosol from Ozonolysis of β-Caryophyllene: Measurements, Predictions, and Implications, ACS Earth and Space Chemistry, 5, 305-318, 10.1021/acsearthspacechem.0c00296, 2021.

Matsunaga, A. and Ziemann, P. J.: Gas-wall partitioning of organic compounds in a Teflon film chamber and potential effects on reaction product and aerosol yield measurements, Aerosol Sci. Technol., 44, 881-892, 10.1080/02786826.2010.501044, 2010.

McDonald, B. C., de Gouw, J. A., Gilman, J. B., Jathar, S. H., Akherati, A., Cappa, C. D., Jimenez, J. L., Lee-Taylor, J., Hayes, P. L., McKeen, S. A., Cui, Y. Y., Kim, S.-W., Gentner, D. R., Isaacman-VanWertz, G., Goldstein, A. H., Harley, R. A., Frost, G. J., Roberts, J. M., Ryerson, T. B., and Trainer, M.: Volatile chemical products emerging as largest petrochemical source of urban organic emissions, Science, 359, 760, 2018.

Mu, Q., Shiraiwa, M., Octaviani, M., Ma, N., Ding, A., Su, H., Lammel, G., Pöschl, U., and Cheng, Y.: Temperature effect on phase state and reactivity controls atmospheric multiphase chemistry and transport of PAHs, Science Advances, 4, eaap7314, 2018.

Nannoolal, Y., Rarey, J., and Ramjugernath, D.: Estimation of pure component properties - Part 3. Estimation of the vapor pressure of non-electrolyte organic compounds via group contributions and group interactions, Fluid Phase Equilibria, 269, 117-133, 10.1016/j.fluid.2008.04.020, 2008.

O'Brien, R. E., Li, Y., Kiland, K. J., Katz, E. F., Or, V. W., Legaard, E., Walhout, E. Q., Thrasher, C., Grassian, V. H., DeCarlo, P. F., Bertram, A. K., and Shiraiwa, M.: Emerging investigator series: chemical and physical properties of organic mixtures on indoor surfaces during HOMEChem, Environmental Science: Processes & Impacts, 23, 559-568, 10.1039/D1EM00060H, 2021.

Pankow, J. F.: An absorption-model of the gas aerosol partitioning involved in the formation of secondary organic aerosol, Atmos. Environ., 28, 189-193, 1994.

719   Petters, S. S., Kreidenweis, S. M., Grieshop, A. P., Ziemann, P. J., and Petters, M. D.:
720   Temperature- and Humidity-Dependent Phase States of Secondary Organic Aerosols,
721   Geophysical Research Letters, 46, 1005-1013, 10.1029/2018GL080563, 2019.

722   Pöschl, U. and Shiraiwa, M.: Multiphase Chemistry at the Atmosphere–Biosphere Interface
723   Influencing Climate and Public Health in the Anthropocene, Chemical Reviews, 115, 4440–
724   4475, 10.1021/cr500487s, 2015.

725   Praske, E., Otkjær, R. V., Crounse, J. D., Hethcox, J. C., Stoltz, B. M., Kjaergaard, H. G., and
726   Wennberg, P. O.: Atmospheric autoxidation is increasingly important in urban and suburban
727   North America, Proc. Nat. Acad. Sci., 115, 64-69, 10.1073/pnas.1715540115, 2018.

728   Presto, A. A., Miracolo, M. A., Donahue, N. M., and Robinson, A. L.: Secondary organic
729   aerosol formation from high-NOx photo-oxidation of low volatility precursors: n-alkanes,
730   Environ. Sci. Technol., 44, 2029-2034, 10.1021/es903712r, 2010.

731   Pye, H. O. T., D'Ambro, E. L., Lee, B. H., Schobesberger, S., Takeuchi, M., Zhao, Y., Lopez-
732   Hilfiker, F., Liu, J., Shilling, J. E., Xing, J., Mathur, R., Middlebrook, A. M., Liao, J., Welti,
733   A., Graus, M., Warneke, C., de Gouw, J. A., Holloway, J. S., Ryerson, T. B., Pollack, I. B., and
734   Thornton, J. A.: Anthropogenic enhancements to production of highly oxygenated molecules
735   from autoxidation, Proc. Nat. Acad. Sci., 116, 6641, 10.1073/pnas.1810774116, 2019.

736   Ranney, A. P., Longnecker, E. R., Ziola, A. C., and Ziemann, P. J.: Measured and Modeled
737   Secondary Organic Aerosol Products and Yields from the Reaction of n-Hexadecane +
738   OH/NOx, ACS Earth and Space Chemistry, 7, 2298-2310,
739   10.1021/acsearthspacechem.3c00227, 2023.

740   Reid, J. P., Bertram, A. K., Topping, D. O., Laskin, A., Martin, S. T., Petters, M. D., Pope, F.
741   D., and Rovelli, G.: The viscosity of atmospherically relevant organic particles, Nature
742   Communications, 9, 956, 10.1038/s41467-018-03027-z, 2018.

743   Renbaum-Wolff, L., Grayson, J. W., Bateman, A. P., Kuwata, K., Sellier, M., Murray, B. J.,
744   Schilling, J. E., Martin, S. T., and Bertram, A. K.: Viscosity of α-pinene secondary organic
745   material and implications for particle growth and reactivity, Proceedings of the National
746   Academy of Sciences of the United States of America, 110, 8014-8019,
747   10.1073/pnas.1219548110 2013.

748   Robinson, A. L., Donahue, N. M., Shrivastava, M. K., Weitkamp, E. A., Sage, A. M., Grieshop,
749   A. P., Lane, T. E., Pierce, J. R., and Pandis, S. N.: Rethinking organic aerosols: Semivolatile
750   emissions and photochemical aging, Science, 315, 1259-1262, 10.1126/science.1133061, 2007.

751   Rothfuss, N. E. and Petters, M. D.: Influence of Functional Groups on the Viscosity of Organic
752   Aerosol, Environ. Sci. Technol., 51, 271-279, 10.1021/acs.est.6b04478, 2017.

753   Saukko, E., Lambe, A. T., Massoli, P., Koop, T., Wright, J. P., Croasdale, D. R., Pedernera, D.
754   A., Onasch, T. B., Laaksonen, A., Davidovits, P., Worsnop, D. R., and Virtanen, A.: Humidity-
755   dependent phase state of SOA particles from biogenic and anthropogenic precursors,
756   Atmospheric Chemistry and Physics, 12, 7517-7529, 10.5194/acp-12-7517-2012, 2012.

757   Schervish, M. and Shiraiwa, M.: Impact of phase state and non-ideal mixing on equilibration
758   timescales of secondary organic aerosol partitioning, Atmos. Chem. Phys., 23, 221-233,
759   10.5194/acp-23-221-2023, 2023.

Seinfeld, J. H. and Pandis, S. N.: Atmospheric chemistry and physics: from air pollution to climate change, John Wiley & Sons2016.

Shiraiwa, M. and Pöschl, U.: Mass accommodation and gas–particle partitioning in secondary organic aerosols: dependence on diffusivity, volatility, particle-phase reactions, and penetration depth, Atmos. Chem. Phys., 21, 1565-1580, 10.5194/acp-21-1565-2021, 2021.

Shiraiwa, M., Ammann, M., Koop, T., and Pöschl, U.: Gas uptake and chemical aging of semisolid organic aerosol particles, Proc. Nat. Acad. Sci., 108, 11003-11008, 10.1073/pnas.1103045108, 2011.

Shiraiwa, M., Berkemeier, T., Schilling-Fahnestock, K. A., Seinfeld, J. H., and Pöschl, U.: Molecular corridors and kinetic regimes in the multiphase chemical evolution of secondary organic aerosol, Atmos. Chem. Phys., 14, 8323-8341, 10.5194/acp-14-8323-2014, 2014.

Shiraiwa, M., Yee, L. D., Schilling, K. A., Loza, C. L., Craven, J. S., Zuend, A., Ziemann, P. J., and Seinfeld, J. H.: Size distribution dynamics reveal particle-phase chemistry in organic aerosol formation, Proceedings of the National Academy of Sciences of the United States of America, 110, 11746-11750, 10.1073/pnas.1307501110, 2013.

Shiraiwa, M., Li, Y., Tsimpidi, A. P., Karydis, V. A., Berkemeier, T., Pandis, S. N., Lelieveld, J., Koop, T., and Pöschl, U.: Global distribution of particle phase state in atmospheric secondary organic aerosols, Nature Communications, 8, 15002, 10.1038/ncomms15002, 2017.

Shrivastava, M., Lou, S., Zelenyuk, A., Easter, R. C., Corley, R. A., Thrall, B. D., Rasch, P. J., Fast, J. D., Massey Simonich, S. L., Shen, H., and Tao, S.: Global long-range transport and lung cancer risk from polycyclic aromatic hydrocarbons shielded by coatings of organic aerosol, Proc. Nat. Acad. Sci., 114, 1246-1251, 2017.

Smith, N. R., Crescenzo, G. V., Huang, Y., Hettiyadura, A. P. S., Siemens, K., Li, Y., Faiola, C. L., Laskin, A., Shiraiwa, M., Bertram, A. K., and Nizkorodov, S. A.: Viscosity and liquid–liquid phase separation in healthy and stressed plant SOA, Environmental Science: Atmospheres, 1, 140-153, 10.1039/D0EA00020E, 2021.

Song, M., Maclean, A. M., Huang, Y., Smith, N. R., Blair, S. L., Laskin, J., Laskin, A., DeRieux, W. S. W., Li, Y., Shiraiwa, M., Nizkorodov, S. A., and Bertram, A. K.: Liquid–liquid phase separation and viscosity within secondary organic aerosol generated from diesel fuel vapors, Atmos. Chem. Phys., 19, 12515-12529, 10.5194/acp-19-12515-2019, 2019.

Srivastava, D., Vu, T. V., Tong, S., Shi, Z., and Harrison, R. M.: Formation of secondary organic aerosols from anthropogenic precursors in laboratory studies, npj Climate and Atmospheric Science, 5, 22, 10.1038/s41612-022-00238-6, 2022.

Tobias, H. J., Kooiman, P. M., Docherty, K. S., and Ziemann, P. J.: Real-Time Chemical Analysis of Organic Aerosols Using a Thermal Desorption Particle Beam Mass Spectrometer, Aerosol Sci. Technol., 33, 170-190, 10.1080/027868200410912, 2000.

Valorso, R., Aumont, B., Camredon, M., Raventos-Duran, T., Mouchel-Vallon, C., Ng, N. L., Seinfeld, J. H., Lee-Taylor, J., and Madronich, S.: Explicit modelling of SOA formation from α-pinene photooxidation: sensitivity to vapour pressure estimation, Atmospheric Chemistry and Physics, 11, 6895-6910, 10.5194/acp-11-6895-2011, 2011.

Vereecken, L. and Peeters, J.: Decomposition of substituted alkoxy radicals—part I: a generalized structure–activity relationship for reaction barrier heights, Physical Chemistry Chemical Physics, 11, 9062-9074, 2009.

Verwer, J. G.: Gauss–Seidel iteration for stiff ODEs from chemical kinetics, SIAM Journal on Scientific Computing, 15, 1243-1250, 1994.

Verwer, J. G., Blom, J. G., and Hundsdorfer, W.: An implicit-explicit approach for atmospheric transport-chemistry problems, Applied Numerical Mathematics, 20, 191-209, 1996.

Virtanen, A., Joutsensaari, J., Koop, T., Kannosto, J., YliPirilä, P., Leskinen, J., Mäkelä, J. M., Holopainen, J. K., Pöschl, U., Kulmala, M., Worsnop, D. R., and Laaksonen, A.: An amorphous solid state of biogenic secondary organic aerosol particles, Nature, 467, 824-827, doi:10.1038/nature09455, 2010.

Ye, Q., Robinson, E. S., Ding, X., Ye, P., Sullivan, R. C., and Donahue, N. M.: Mixing of secondary organic aerosols versus relative humidity, Proc. Nat. Acad. Sci., 113, 12649-12654, 2016.

Zaveri, R. A., Wang, J., Fan, J., Zhang, Y., Shilling John, E., Zelenyuk, A., Mei, F., Newsom, R., Pekour, M., Tomlinson, J., Comstock Jennifer, M., Shrivastava, M., Fortner, E., Machado Luiz, A. T., Artaxo, P., and Martin Scot, T.: Rapid growth of anthropogenic organic nanoparticles greatly alters cloud life cycle in the Amazon rainforest, Science Advances, 8, eabj0329, 10.1126/sciadv.abj0329, 2022.

Zhang, X., Cappa, C. D., Jathar, S. H., McVay, R. C., Ensberg, J. J., Kleeman, M. J., and Seinfeld, J. H.: Influence of vapor wall loss in laboratory chambers on yields of secondary organic aerosol, Proc. Nat. Acad. Sci., 111, 5802-5807, 2014.

Zhang, Y., Chen, Y., Lambe, A. T., Olson, N. E., Lei, Z., Craig, R. L., Zhang, Z., Gold, A., Onasch, T. B., Jayne, J. T., Worsnop, D. R., Gaston, C. J., Thornton, J. A., Vizuete, W., Ault, A. P., and Surratt, J. D.: Effect of the Aerosol-Phase State on Secondary Organic Aerosol Formation from the Reactive Uptake of Isoprene-Derived Epoxydiols (IEPOX), Environmental Science & Technology Letters, 5, 167-174, 10.1021/acs.estlett.8b00044, 2018.

Zhang, Y., Nichman, L., Spencer, P., Jung, J. I., Lee, A., Heffernan, B. K., Gold, A., Zhang, Z., Chen, Y., Canagaratna, M. R., Jayne, J. T., Worsnop, D. R., Onasch, T. B., Surratt, J. D., Chandler, D., Davidovits, P., and Kolb, C. E.: The Cooling Rate- and Volatility-Dependent Glass-Forming Properties of Organic Aerosols Measured by Broadband Dielectric Spectroscopy, Environ. Sci. Technol., 53, 12366-12378, 10.1021/acs.est.9b03317, 2019.

Zhao, B., Wang, S., Donahue, N. M., Jathar, S. H., Huang, X., Wu, W., Hao, J., and Robinson, A. L.: Quantifying the effect of organic aerosol aging and intermediate-volatility emissions on regional-scale aerosol pollution in China, Sci. Rep., 6, 28815, 10.1038/srep28815, 2016.

Zhou, S., Hwang, B. C. H., Lakey, P. S. J., Zuend, A., Abbatt, J. P. D., and Shiraiwa, M.: Multiphase reactivity of polycyclic aromatic hydrocarbons is driven by phase separation and diffusion limitations, Proc. Nat. Acad. Sci., 116, 11658-11663, 10.1073/pnas.1902517116, 2019.

Ziemann, P. J. and Atkinson, R.: Kinetics, products, and mechanisms of secondary organic aerosol formation, Chemical Society Reviews, 41, 6582-6605, 2012.

841   Zobrist, B., Marcolli, C., Pedernera, D. A., and Koop, T.: Do atmospheric aerosols form
842   glasses?, Atmospheric Chemistry and Physics, 8, 5221-5244, 2008.
843
844

 Appendix.

846

847 **Table A1:** Experimental and simulated functional group distributions, O:C and N:C ratios of

848 SOA generated from C16 oxidation by OH in presence of high NO_x.

FG/C16 molecule	Experimental	Simulated (tgBoost)	Simulated (CP)
Nitrate	0.91	0.65	0.54
Carbonyl	0.38	0.26	0.15
Hydroxyl	0.41	0.43	0.45
Carboxyl	0.09	0.0	0.0
Ester	0.28	0.2	0.07
Peroxide	0.12	0.01	0.0
Methylene	13.81	12.12	12.07
O:C	0.28	0.25	0.25
N:C	0.06	0.04	0.03
H:C	1.85	/	/
MW	294	/	/
Density (g cm^{-3})	1.10	1.06	1.06

849

850

851
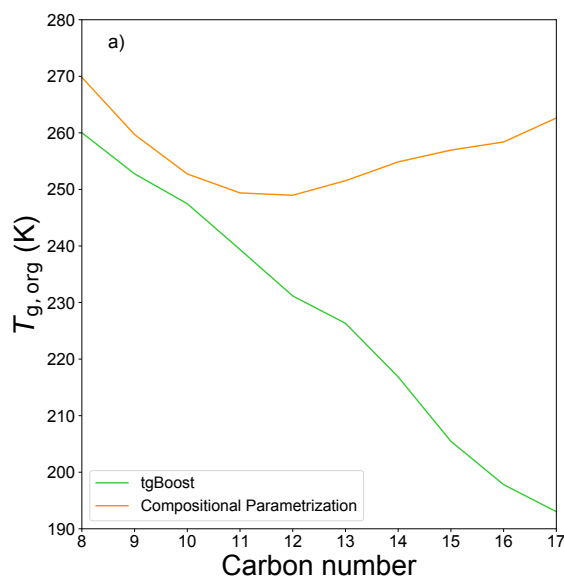
852

853 **Figure A1:** Predicted $T_{g,org}$ of SOA generated from n-alkanes as computed by the GECKO-A

854 box model with the T_g compositional parametrization (orange line) and tgBoost (green line) at

855 the last step of the simulations (t = 3600 s).

856

CP = 272 K (3x10^{-2})
tgBoost = 195 K (0.99)
1st gen.

CP = 267 K (0.78)
tgBoost = 201 K (1.0)
1st gen.

CP = 225 K (2x10^{-3})
tgBoost = 165 K (0.86)
2nd gen.

CP = 261 K (6x10^{-3})
tgBoost = 196 K (0.99)
1st gen.

CP = 261 K (0.14)
tgBoost = 179 K (1.0)
1st gen.

CP = 281 K (1x10^{-2})
tgBoost = 180 K (0.99)
2nd gen.

CP = 260 K (1x10^{-2})
tgBoost = 186 K (0.99)
2nd gen.

CP = 268 K (0.74)
tgBoost = 230 K (1.0)
3rd gen.

CP = 266 K (0.97)
tgBoost = 239 K (1.0)
2nd gen.

CP = 281 K (2x10^{-2})
tgBoost = 188 K (0.99)
2nd gen.

CP = 265 K (0.65)
tgBoost = 221 K (1.0)
2nd gen.

CP = 263 K (0.16)
tgBoost = 205 K (1.0)
2nd gen.

CP = 287 K (0.41)
tgBoost = 198 K (1.0)
3rd gen.

CP = 263 K (0.16)
tgBoost = 211 K (1.0)
2nd gen.

CP = 265 K (2x10^{-4})
tgBoost = 249 K (0.88)
3rd gen.

Figure A2. Top 15 species with highest concentrations in oxidation products of n-hexadecane ($C_{16}H_{34}$) under high NOx conditions simulated by GECKO-A with effective mass accommodation coefficient (α_{eff}) with the compositional parameterization. The species are reported in descending concentrations from left to right and from top to bottom. Listed values are T_g as calculated by tgBoost and CP and α_{eff} values at the end of simulation (3600 s) in brackets. Types of compounds are also noted (1st, 2nd, and 3rd generation products, decomposition products).
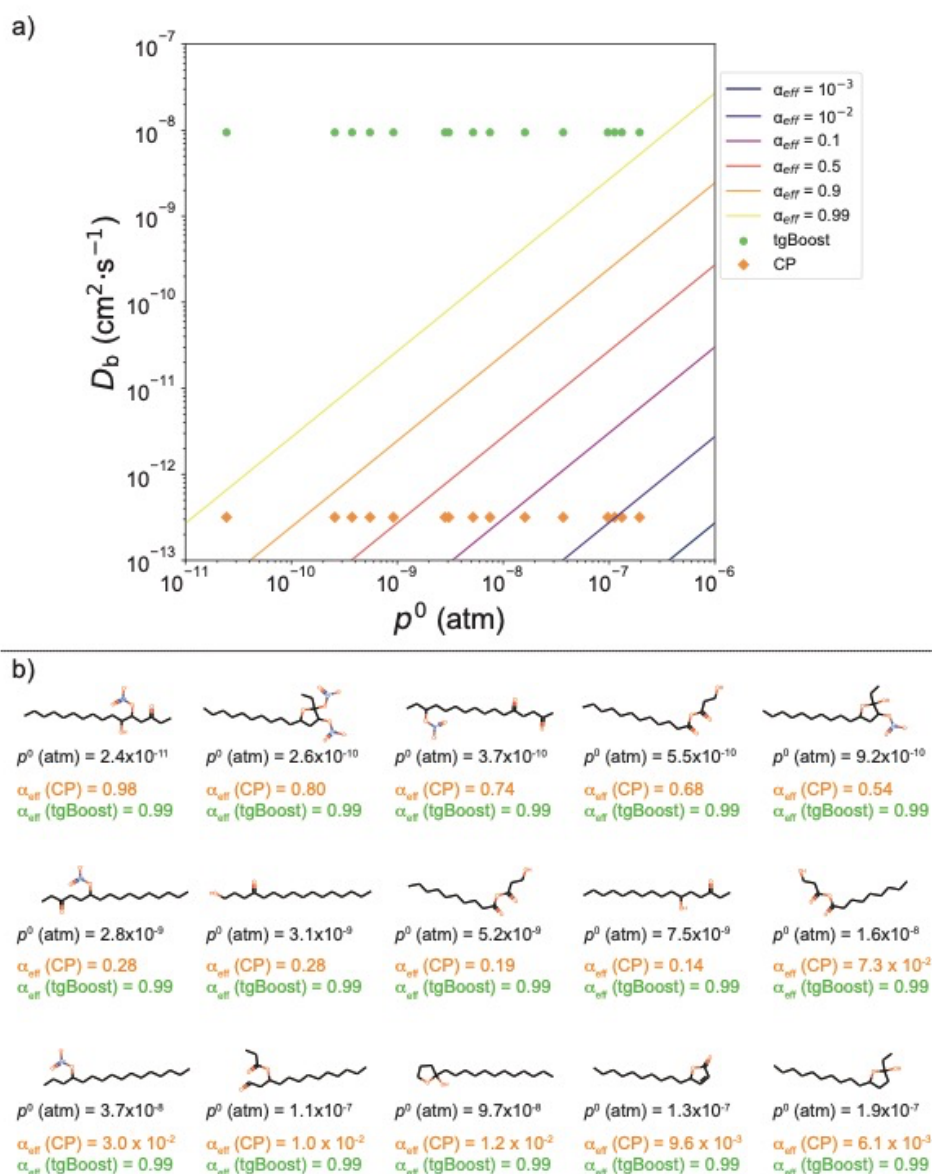
Figure A3. a) α_{eff} isolines as a function of bulk diffusivity D_{b} and saturation vapor pressure p^{o} of semi-volatile species. b) Selection of various representative SOA contributors produced during the oxidation of n-hexadecane. The species are ordered by decreasing vapor pressure. The reported α_{eff} values for each SOA contributor are calculated for D_{b} estimated with tgBoost ($D_{\mathrm{b}} = 1\times10^{-8}$ cm^2 s^{-1}) and CP ($D_{\mathrm{b}} = 3\times10^{-13}$ cm^2 s^{-1}). The values of α_{eff} for the selected species are reported as points in the top panel. It shows that for the liquid-like state estimated with the tgBoost configuration, α_{eff} tend towards 1 for all species. This behavior is not observed in the amorphous semi-solid state estimated using the CP model configuration for species with p^{o} above 10^{-9} atm. For the simulated conditions, species with p^{o} between 10^{-8} and 10^{-6} atm are of enough low volatility to partition between the particle and gas phases at equilibrium. For species in that volatility range, no mass transfer limitation is observed with the tgBoost configuration, unlike the CP configuration. Using the CP configuration, the most volatile SOA contributors are subjected to substantial mass transfer limitation and are therefore mainly eliminated by gas-phase oxidation or wall deposition.